

Investigating the Influence of Spatial Constraints on Ultimate Receive Coil Performance for Monkey Brain MRI at 7T

Yang Gao, Weidao Chen, and Xiaotong Zhang*

Abstract—The RF receive coil array has become increasingly vital in current MR imaging practice due to its extended spatial coverage, maintained high SNR, and improved capability of accelerating data acquisition. The performance of a coil array is intrinsically determined by the current patterns generated in coil elements as well as by the induced electromagnetic fields inside the object. Investigations of the ultimate performance constrained by a specific coil space, which defines all possible current patterns flowing within, offers the opportunity to evaluate coil-space parameters (i.e., coverage, coil-to-object distance, layer thickness, and coil element type) without the necessity of considering the realistic coil element geometry, coil elements layout, and number of receive channels in modeling. In this study, to mimic 7T monkey RF head coil design, seven hypothetical ultimate coil arrays with different coil-space configurations were mounted over a numerical macaque head model; by using Huygens's surface approximation method, the influences of coil-space design parameters were systematically investigated through evaluating the spatial constrained ultimate intrinsic SNR (UISNR) and ultimate g-factor (uGF). Moreover, simulations were also conducted by using four coil arrays with limited number of loop-only elements, in order to explore to what extent, the ultimate coil performance can be achieved by using practical coil designs, and hence several guidelines in RF coil design for monkey brain imaging at 7T have been tentatively concluded. It is believed that the present analysis will offer important implications in novel receive array design for monkey brain MR imaging at UHF.

Index Terms—MRI, RF receive coil, ultimate Intrinsic SNR (UISNR), ultimate G-factor (uGF), coil space, spatial constraints, electromagnetic simulation, monkey brain imaging, ultra-high field (UHF)

I. INTRODUCTION

MR brain imaging is a non-invasive and important means for the investigation of tissue anatomy and neuronal activities [1-5]. For the purposes of studying column-like functional structures [6-10], discriminating layer-specific BOLD responses [11-13], and exploring neurovascular coupling [14-16], submillimeter-resolution functional imaging and anatomical references are required. While single-channel

and small-diameter loop coil has been playing an important role in initial efforts to pursue submillimeter neuroimaging [17-19], parallel imaging with receive coil array has become more popular in current imaging practice due to its extended spatial coverage, maintained high SNR, and improved capability of accelerating data acquisition which plays a key role in high spatial- and temporal-resolution acquisition [20-24]. Up to now, the main efforts to improve receive sensitivity has been dedicated to shortening coil-to-object distance as well as to increasing the number of receive channels. For example, close-fitted human head coil with massive parallel receive channels and whole-head coverage has demonstrated its high SNR and improved acceleration performance with increased channels [20,22]. However, in monkey brain imaging, thick temporal muscles and various demands such as head fixation, surgery, compatibility with other imaging modality limit the minimum distance between coil and monkey brain; besides, for such practical issues, coil design with massive receive array is usually difficult to achieve a whole-head coverage and thus affects the overall performance [25]. There have been a number of studies trying to resolve above challenges. Considering the fact that different monkey head sizes may inevitably lead to SNR drop because of sub-optimized distance between coil and head, a variety of specialized close-fitted designs have been proposed [26-29] to fit to individual monkeys, and novel flexible coil has been designed to fit to monkeys with different head sizes [30]. Besides, to further shorten the distance between the coil and the region of interest, invasive implanted coil arrays have demonstrated their superior performances as compared with non-invasive head coil arrays [31-33]. Moreover, novel designs based on complex combination of coil array parameters (i.e., coil-space coverage, coil-to-object distance, coil element type, etc.) have been utilized; for example, multiple receive arrays with different coil-space coverages and coil-to-object distances (multiple layers) have been proposed to achieve locally high SNR and a whole-head coverage [26,29]. Recently, both numerical simulation studies and experimental results suggested that using loop coil element alone only achieves sub-optimal SNR as compared with what the ultra-high field (UHF)

Copyright (c) 2017 IEEE. Personal use of this material is permitted. However, permission to use this material for any other purposes must be obtained from the IEEE by sending a request to pubs-permissions@ieee.org.

This work was supported in part by National Natural Science Foundation of China (81701774, 61771423, 61671405) and Fundamental Research Funds for the Central Universities (2016QN81018), China. Asterisk indicates the corresponding author.

Y. Gao, W. Chen and X. Zhang* are with the Interdisciplinary Institute of Neuroscience and Technology, Qiushi Academy for Advanced Studies, and the Key Laboratory for Biomedical Engineering of Ministry of Education, College of Biomedical Engineering & Instrument Science, both at Zhejiang University, Hangzhou, China.

can inherently reach [34-39].

In order to achieve higher SNR and better inverse g-factor – the latter as the measure of the acceleration performance in MRI data acquisition – previous endeavor in finding the optimal receive array design focused on parameters such as the number of channels, overlap between elements, and elements arrangement within the coil space [40-43], but parameters of, i.e., coil-to-object distance, coil-space coverage, coil element type, and coil-space thickness have been rarely studied in a systematical way, whereas these parameters may play a more determinant role in monkey head receive array design as compared with the human head coil design.

To evaluate the role of aforementioned design parameters, traditional simulation methods on receive coil array using realistic coil elements are not optimal due to their difficulties in eliminating the influence of coil elements arrangement as well as the receive channel numbers on the coil performance. In contrast, the simulation of the ultimate performances (i.e., ultimate intrinsic SNR – UISNR, and ultimate intrinsic g-factor – uGF) of the coil array under the constraint of electrodynamics [44,45] appears to be more feasible in investigating the influence of coil-space coverage, coil-object distance, coil-element type, and coil-space thickness, because it covers the optimized coil elements arrangement and deals with infinite large number of receive channel numbers. Recently, Dyadic Green Function (DGF) based analytical ultimate intrinsic SNR calculation method has been proposed, providing a mathematical and time-efficient link between electric current patterns and electromagnetic (EM) fields [46,47], and thus it becomes feasible to explore the influence of coil-element type (electric current type) on uniform spheres and cylinders. But closed spherical or cylindrical surfaces are usually required in simulating the ultimate coil performance in DGF method. According to the Huygens's equivalent principle, the ultimate performance is independent of the geometry of closed Huygens's equivalent electric current surface and its distance from the object [48]; however, for realistic coil arrays, it is not practical to make the coil geometry closed and a conformal surface is usually adopted to shorten the coil-to-object distance for head imaging, so the DGF-based approach may not be suitable to connect the ultimate performance with practical coil design. Most recently, a promising numerical simulation method for the ultimate performance with novel electric current basis set has been proposed to apply to realistic-geometry models and be capable of forming opened equivalent electric current surfaces over conformal surfaces, which is equivalent to putting spatial constraints on the canonical Huygens's equivalent surface [49,50], and similar UISNR profiles and conclusions are drawn using these two methods. The necessity of using opened conformal surface to investigate ultimate coil performance still requires further validation. In addition, the influence of coil-space coverage and coil-to-object distance on ultimate coil performance has yet been compared.

In the present study, over a numerical macaque head model, seven coil arrays with different coil-space configurations were constructed to mimic monkey head MRI at 7T, and by using Huygens's surface approximation method, the influences of

coil-space design parameters, i.e., the coil-space coverage, coil-to-object distance, coil-element type, as well as the coil-space thickness, have been systematically investigated through evaluating the corresponding UISNR and uGF. Additional simulations were also conducted by using four coil arrays with limited number of loop-only elements, in order to explore to what extent, the ultimate coil performance can be achieved by using practical coil designs. It is believed that the present analysis will offer important implications in novel receive array design for monkey brain MR imaging at UHF.

II. THEORY AND METHOD

A. Spatial Constrained UISNR and uGF

The solution to Maxwell equations on a linear object forms a linear space. Therefore, the electrodynamic constraints on intrinsic SNR can be translated directly to the hypothetical net coil (a concept in SENSE reconstruction method [51]), which is a linear combination of actual coils [45]. Under the ultimate case, all possible EM fields generated by the hypothetical ultimate net coil with acceleration rate N at each voxel \mathbf{r}_ρ ($\rho=0, \dots, N$, and $\rho > 0$ represents aliasing voxel position under SENSE acceleration) can be linearly combined with complete basis of EM basis:

$$\mathbf{E}^{net,\rho}(\mathbf{r}) = \sum w_{\rho,m} \boldsymbol{\alpha}_m(\mathbf{r}) \quad (1)$$

$$\mathbf{H}^{net,\rho}(\mathbf{r}) = \sum w_{\rho,m} \boldsymbol{\beta}_m(\mathbf{r}) \quad (2)$$

where $\boldsymbol{\alpha}_m(\mathbf{r})$, $\boldsymbol{\beta}_m(\mathbf{r})$ are electric and magnetic vector basis functions with index m , respectively, and $w_{\rho,m}$ is complex expansion weighting coefficient.

The intrinsic SNR is inherently determined by the EM fields inside the object. Sample noise is the only type of noise contribution to the intrinsic SNR. The intrinsic SNR per unit of square root receiver bandwidth and unit sample volume is:

$$\text{Intrinsic SNR}(\mathbf{r}) = \frac{\omega M_0 \mathbf{B}_1^-(\mathbf{r})}{\sqrt{4k_B T \int \sigma(\mathbf{r}) |\mathbf{E}(\mathbf{r})|^2 d\mathbf{r}}} \quad (3)$$

where M_0 is the equilibrium magnetization, ω the Larmor frequency, k_B the Boltzmann's constant, and T_s the absolute temperature of the object. \mathbf{B}_1^- is the RF-coil-induced anti-rotating component of transverse magnetic field, which is the source of signal:

$$\mathbf{B}_1^- = \mu_0 \frac{(H_x - iH_y)^*}{2} \quad (4)$$

in which H_x and H_y are the magnetic field strength vector components in the Cartesian coordinate, and μ_0 is the free space permeability (assumed in all aqueous tissues). The net signal sensitivity, which is combined with signals from all EM field basis vectors, in weak SENSE reconstruction (parallel imaging reconstruction method) is set to one at the reconstructed position \mathbf{r}_ρ (when $\rho = \rho'$) and equal to zero at the aliasing positions (when $\rho \neq \rho'$) [45]:

$$H_x^{net,\rho}(\mathbf{r}_{\rho'}) - iH_y^{net,\rho}(\mathbf{r}_{\rho'}) = \delta_{\rho,\rho'} \quad \rho, \rho' = 0, \dots, N \quad (5)$$

Defining the signal sensitivity matrix \mathbf{S} of coil m at pixel position \mathbf{r}_ρ and noise co-variance matrix $\boldsymbol{\Psi}$ of coil m and m' :

$$S_{m,\rho} = H_{m,x}(\mathbf{r}_\rho) - iH_{m,y}(\mathbf{r}_\rho) \quad (6)$$

$$\boldsymbol{\Psi}_{mm'} = \sigma \int \boldsymbol{\alpha}_m(\mathbf{r}) \boldsymbol{\alpha}_{m'}^*(\mathbf{r}) d^3\mathbf{r} \quad (7)$$

By substituting (6), (7) with (1) (2) (4) and (5), the signal component and noise component in SNR equation (3) can be written in the linear form (8) and (9):

$$\mathbf{W}\mathbf{S} = \mathbf{I}d, \quad (8)$$

$$\int \sigma |\mathbf{E}^{net,\rho}(\mathbf{r})|^2 d^3r = (\mathbf{W}\mathbf{\Psi}\mathbf{W}^H)_{\rho,\rho'} \quad (9)$$

where $\mathbf{I}d$ denotes the $(N+1) \times (N+1)$ identity matrix.

By substituting (3) with (8) and (9) and omit the constant, the intrinsic SNR can be written as the function of expansion weighting coefficient \mathbf{W} and noise-covariance matrix $\mathbf{\Psi}$:

$$\text{Intrinsic SNR} = \frac{1}{\sqrt{\mathbf{W}\mathbf{\Psi}\mathbf{W}^H}} \quad (10)$$

It is noteworthy that all SNR calculated in this study is intrinsic SNR, which is independent of the imaging parameters and signal processing system.

Under the constraint of weak SENSE reconstruction, the optimal weighting coefficient \mathbf{W}_{opt} can be derived through solving constrained linear optimization problem [45].

$$\mathbf{W}_{opt} = (\mathbf{S}^H \mathbf{\Psi}^{-1} \mathbf{S})^{-1} \mathbf{S}^H \mathbf{\Psi}^{-1} \quad (11)$$

The optimized intrinsic SNR with specific EM field basis set can be derived with optimal weighting coefficient \mathbf{W}_{opt} . Combining (10) and (11), optimal intrinsic SNR can be written as the function of \mathbf{S} and $\mathbf{\Psi}$:

$$\text{SNR}_{opt} = \frac{1}{\sqrt{(\mathbf{S}^H \mathbf{\Psi}^{-1} \mathbf{S})^{-1}}} \quad (12)$$

The ultimate intrinsic SNR is approached and calculated with a large number of complete EM basis fields.

The analytical expression of the ultimate g-factor can also be derived based on SENSE parallel imaging reconstruction method [51], thus is not described here. The noise co-variance matrix was excluded from g-factor calculation in this study to mimic the effect of ideal decoupling. In addition, “worst case g-factor” was ensured and compared through cropping the image field of view (FOV) to fit the nonzero head voxels. A large number of complete EM basis fields are required to approach ultimate intrinsic g-factor.

According to the Huygens’s equivalence principle, any EM field distributions inside a closed volume devoid of sources can be generated by a current distribution flowing on the surface defining that volume [48]. The electric current flowing on the outer surface (coil space) and the resultant EM fields inside a closed volume (object space) are constrained by electrodynamics. Therefore, UISNR can be derived from both complete electric current basis set (12) and complete EM field basis set (17).

For closed spherical equivalent electric current surfaces, sensitivity matrix \mathbf{X} and noise covariance matrix \mathbf{P} derived from complete EM field basis set can be translated into sensitivity matrix \mathbf{S} and noise covariance matrix $\mathbf{\Psi}$ derived from the complete electric current basis set by using transformation matrix \mathbf{T} [46], which stands for boundary conditions over the spherical Huygens’s surface:

$$\mathbf{S} = \mathbf{T}\mathbf{X} \quad (13)$$

$$\mathbf{\Psi} = \mathbf{T}\mathbf{P}\mathbf{T}^H \quad (14)$$

The transformation matrix \mathbf{T} in DGF-based method [46] using spherical Huygens’s surface is written in the following form:

$$\mathbf{T} = \begin{bmatrix} -i\sqrt{l(l+1)}h_l^{(1)}(k_0b)C_l & 0 \\ 0 & \frac{-i\sqrt{l(l+1)}}{k_0b} \frac{\partial [r h_l^{(1)}(k_0r)]}{\partial r} \Big|_{r=b} D_l \end{bmatrix} \quad (15)$$

$h_l^{(1)}$ is the spherical Hankel function of the first kind of order l and the complete wave number outside the sphere is calculated as $k_0^2 = \omega^2 \mu_0 \mu_0 \epsilon_0$. The coefficients C_l and D_l in the matrix \mathbf{T} are determined by applying Dirichlet boundary conditions at the surface of the sphere with radius b .

Then, UISNR derived from the complete electric current basis set (12) can be transformed to UISNR derived from complete EM field basis set (17) through equation (16) [37]:

$$\begin{aligned} \mathbf{S}^H \mathbf{\Psi}^{-1} \mathbf{S} &= (\mathbf{T}\mathbf{X})^H (\mathbf{T}\mathbf{P}\mathbf{T}^H)^{-1} (\mathbf{T}\mathbf{X}) \\ &= \mathbf{X}^H \mathbf{T}^H (\mathbf{T}^H)^{-1} \mathbf{P}^{-1} \mathbf{T}^{-1} \mathbf{T}\mathbf{X} \\ &= \mathbf{X}^H \mathbf{P}^{-1} \mathbf{X} \end{aligned} \quad (16)$$

$$\text{SNR}_{opt} = \frac{1}{\sqrt{(\mathbf{X}^H \mathbf{P}^{-1} \mathbf{X})^{-1}}} \quad (17)$$

Because UISNR constrained by object space (17) is independent of the boundary condition of coil space, UISNR constrained by closed coil space (i.e. canonical Huygens’s surface) is also independent of coil-to-object distance, which is one boundary condition of coil space and defined in transformation matrix \mathbf{T} .

Now we explore whether UISNR is dependent of coil-to-object distance when spatial constraints are imposed on Huygens’s equivalent surface. Ideal circular surface loop coil constructed through spatial constraint of current basis set was described in [46], in which the surface current distribution was defined for a loop coil of radius R positioned outside the dielectric sphere, with its axis along the z-direction and a distance d from the center of the sphere:

$$\mathbf{K}_z^{open}(\theta, \phi) = \mathbf{I} \frac{\sin\theta}{\sqrt{d^2 + R^2}} \delta(r - \sqrt{d^2 + R^2}) \delta(\cos\theta - \frac{d}{\sqrt{d^2 + R^2}}) \quad (18)$$

where \mathbf{I} is the current flowing in the coil. The radius b of the boundary of the current flowing surface equals to $\sqrt{d^2 + R^2}$. Both spatial constraint $\delta(r - \sqrt{d^2 + R^2})$ and $\delta(\cos\theta - \frac{d}{\sqrt{d^2 + R^2}})$ define the geometry and spatial location of the circular loop coil.

The current distribution of the loop coil can also be expressed as a weighted combination of the magnetic current basis functions:

$$\mathbf{K}_z^{open}(\theta, \phi) = \sum_{l=0}^{\infty} \sum_{m=-l}^{+l} W_{l,m}^M [-i\sqrt{l(l+1)}\mathbf{X}_{l,m}(\theta, \phi)] \quad (19)$$

Because equation (18) and (19) are the same, the weighting coefficient $W_{l,m}^M$ can be derived as:

$$\begin{aligned} W_{l,m}^M &= \frac{-2\pi R}{(l+1)} \left[\cot\theta Y_l^0(\theta, \phi) - \right. \\ &\left. \csc\theta \sqrt{\frac{2l+1}{2l-1}} Y_{l-1}^0(\theta, \phi) \right]_{\theta=\cos^{-1}\frac{d}{b}} \end{aligned} \quad (20)$$

Combining equation (10) and (14), intrinsic SNR of a circular loop can be written as:

$$\text{Intrinsic SNR} = \frac{1}{\sqrt{\mathbf{W}\mathbf{T}\mathbf{P}(\mathbf{W}\mathbf{T})^H}} \quad (21)$$

$$W_{l,m}^M T_{l,m}^M = \frac{i2\pi R\sqrt{l}}{\sqrt{l+1}} h_l^{(1)}(k_0 b) C_l \left[\cot \theta Y_l^0(\theta, \phi) - \csc \theta \sqrt{\frac{2l+1}{2l-1}} Y_{l-1}^0(\theta, \phi) \right]_{\theta=\cos^{-1}\frac{d}{b}} \quad (22)$$

Noise covariance matrix \mathbf{P} derived from complete EM field basis set is independent of the coil-space constraint, while \mathbf{WT} is determined by the coil-to-object distance d and the coverage of the coil space. Therefore, spatial constrained UISNR is dependent of the coil-space coverage and coil-to-object distance. Considering the coil space is opened in practical coil design, to investigate how such spatial constraints may affect the ultimate coil performance is important and will certainly provide helpful insights and guidance for practical coil array design.

B. EM Field Basis Set

The numerical method for calculating EM field basis set constrained by opened realistic coil-space geometry was firstly devised by Bastien and et. al. [49,50], and is utilized in this study to calculate the EM field basis set over a monkey head model with different coil-space geometries and coil-to-object distances. The numerical approach of calculating the EM field basis set is summarized below:

b1) Computation of incident field basis set using free-space DGFs

The coil space and the monkey head model were discretized and shared the same 2mm isotropic voxel size. Three electric dipoles and three magnetic dipoles (all oriented along x-, y-, and z-axis, respectively) were placed at each discretized location, as depicted in Fig.1(c). The discretized dipole cloud was used to mimic all possible electric current distribution in each specific coil space. The dipole cloud was energized with random magnitudes and phases for multiple excitations. Each electric current basis vector was made up of all dipoles in the dipole cloud, and each dipole was assigned with a random magnitude and phase for each specific excitation. The resultant incident field basis vector of corresponding current basis vector was calculated by using free-space DGFs [52]. 4,000 incident EM fields of magnetic current basis set and 4,000 incident EM fields of electric current basis set were generated through 4,000 random excitations within the dipole cloud.

b2) Computation of total fields

The ultrafast volume integral equation solver – Magnetic Resonance Integral Equation (MARIE) [53] – was used to compute the scattered fields given in the incident fields. Total fields of current basis set (both electric and magnetic currents)

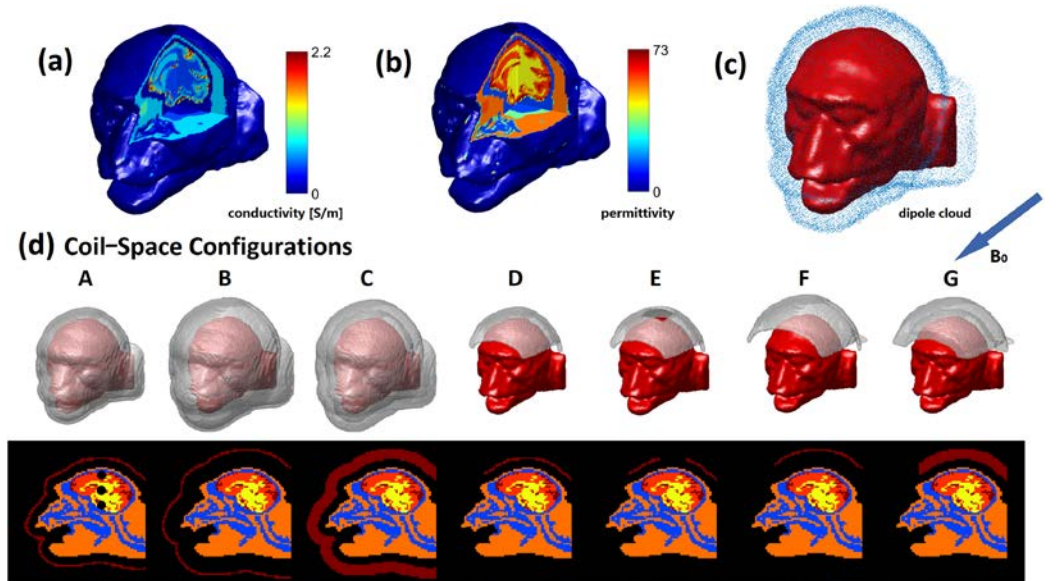


Fig.1. The conductivity (a) and relative permittivity (b) distributions of the realistic macaque head model. The monkey head is enclosed by discretized current distributions on the Huygens' surface using electric and magnetic dipoles (dipole clouds) as shown in (c), and seven coil-space configurations are shown in (d) with their 3D and sagittal views, respectively.

were calculated through the combination of incident fields and scattered fields. All simulations were performed on a Windows server with 368 GB of RAM, Intel Xeon CPU E5-2640 v3 2.6GHz and a Tesla K80 GPU. 4,000 random excitations were utilized (same with [1]) which yielded a computation time (with GPU acceleration) of ~2.5 days per coil-space configuration.

C. Realistic-Geometry Macaque Head Model

MPRAGE T1-weighted MR head images (128×112×96, 1mm isotropic) of an anesthetized macaque were acquired on a 7T research scanner (Siemens Healthcare, Erlangen, Germany). The head images were then segmented into five tissues: scalp, skull, grey matter, white matter, and cerebrospinal fluid (CSF) [54]. The dielectric properties of each tissue were assigned with values of the corresponding human head tissues at 300MHz [55,56], and the distributions of conductivity and relative permittivity are shown in Fig.1(a) and (b), respectively. To reduce the computation load, we sub-sampled the model to 2mm isotropic spatial resolution, resulting in 72,964 tissue voxels. The monkey was assumed to be placed in the prone position inside a horizontal MRI bore, and the direction of main magnetic field is indicated in Fig.1.

D. Coil-space Configuration

Seven coil-space configurations were constructed as shown in Fig.1(d):

A) whole-head coverage but with no dipoles behind the neck, 3mm thickness, and 1cm coil-to-object distance;

B) whole-head coverage (same with A), 3mm thickness, 2cm coil-to-object distance;

C) whole-head coverage (same with A), 13mm thickness, 1cm coil-to-object distance;

D) helmet-like coverage covering only the top head (leaving space for ear-bar and visual stimulus), 3mm thickness, 1cm coil-to-object distance;

E) helmet-like coverage (same with D) but with a 28 mm × 28 mm rectangular coil opening for headpost installation, 3mm thickness, 1cm coil-to-object distance;

F) helmet-like coverage (same with D), 3mm thickness, 2cm coil-to-object distance;

G) helmet-like coverage (same with D), 13mm thickness, 1cm coil-to-object distance.

Configurations A-C were to represent the optimal coil-space coverage and geometry for anesthetized monkey brain imaging, despite the challenges in reproducing the conformal surfaces in reality. The helmet-like configurations D-G were to deliberately mimic the specialized design for anesthetized monkey experiment with ear-bar and bite-bar [25,27], as well as for awake monkey experiment with head-post for head fixation [28,32], respectively; in addition, the coil space with further distance from head was to simulate the condition when the space for coil elements is limited by head-constraint or multi-modal imaging device (e.g., optical probes), and thick layer coil space was to allow electric current flowing at different distance above the head, allowing to explore the potential advantage of using multi-layer coil arrangement [30].

E. Magnetic and Electric Current Contributions to UISNR

The intrinsic SNR generated by the complete current basis set with N basis field vectors is written in Equation (23). The sensitivity matrix (24) and noise co-variance matrix (25) contain both contributions from magnetic and electric current basis sets, respectively:

$$SNR_N^{Complete} = \frac{1}{\sqrt{(S_N^{Complete})^H \Psi_N^{Complete} S_N^{Complete} - 1}} \quad (23)$$

$$S_N^{Complete} = \begin{bmatrix} S_{N/2}^M \\ S_{N/2}^E \end{bmatrix} \quad (24)$$

$$\Psi_N^{Complete} = \begin{bmatrix} \Psi_{N/2}^M & \Psi_{N/2}^{E,M} \\ \Psi_{N/2}^{M,E} & \Psi_{N/2}^E \end{bmatrix} \quad (25)$$

The intrinsic SNRs of electric and magnetic current basis sets follows the definition used in [37], as shown in (26) and (27):

$$SNR_N^M = \frac{1}{\sqrt{(S_N^M)^H \Psi_N^M S_N^M - 1}} \quad (26)$$

$$SNR_N^E = \frac{1}{\sqrt{(S_N^E)^H \Psi_N^E S_N^E - 1}} \quad (27)$$

To evaluate the contributions of two types of current basis sets, we define the current contribution as the ratio of SNR generated by a single type of current basis set

vs. the SNR generated by complete current basis set as in (28) and (29):

$$Contribution_N^M = \frac{SNR_N^M}{SNR_N^{Complete}} \quad (28)$$

$$Contribution_N^E = \frac{SNR_N^E}{SNR_N^{Complete}} \quad (29)$$

The contribution of magnetic and electric current has been systematically investigated on a uniform sphere [37]. In this study, to ensure a fair comparison of ultimate performances of single-type current and complete current, the number of vector basis functions in both numerator and denominator are kept the same. With a sufficient number of basis vectors, the intrinsic SNR of complete current and single current basis should be fully converged as shown in (30), as well as for the contribution index shown in (31):

$$\begin{cases} \lim_{N \rightarrow \infty} SNR_N^{Complete} = UISNR^{Complete} \\ \lim_{N \rightarrow \infty} SNR_N^M = UISNR^M \\ \lim_{N \rightarrow \infty} SNR_N^E = UISNR^E \end{cases} \quad (30)$$

$$\begin{cases} \lim_{N \rightarrow \infty} Contribution_N^M = \frac{UISNR^M}{UISNR^{Complete}} \\ \lim_{N \rightarrow \infty} Contribution_N^E = \frac{UISNR^E}{UISNR^{Complete}} \end{cases} \quad (31)$$

F. Comparison between Magnetic Current and divergence-free current contributions

To verify whether the magnetic current can represent the loop element, we compared the contributions of magnetic current vs. divergence-free current on a uniform spherical model, with the latter derived from the DGF method (the relationship between divergence-free current and the loop element has been well established [46,57,58]). The uniform sphere with a 90mm diameter shared a similar dimension with the monkey head model, and the distance between the electric current surface and the spherical model was 1cm. For the magnetic current contribution, isotropic spatial resolution ranging from 1.5mm to 2.5mm for both head model and dipole cloud were utilized to calculate the divergence-free current contribution. The DGF for divergence-free and curl-free current were expanded on spherical harmonics functions with spatial order $L_{max}=35$, which yielded $2(L_{max}+1)^2-2=2,590$ basis fields. In this study, 4,000 random excitations were used to generate 8,000 basis fields, including 4,000 magnetic current basis fields and 4,000 electric current basis fields.

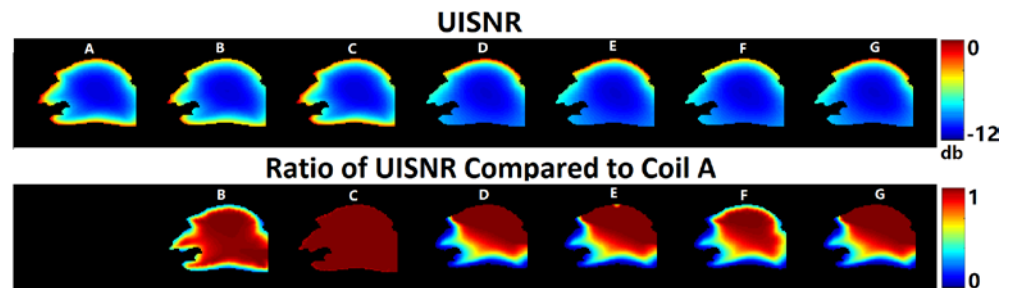


Fig.2. Sagittal views of UISNR maps (natural log scale) for each coil-space configuration (upper row), and the ratio of UISNR for coil configurations B-G compared to coil configuration A (lower row).

G. Approaching the ultimate performance of loop coil arrays

To evaluate to what extent the ultimate coil performance can be approached with finite coil setups, four arrays (I-IV) were modeled consisting of different numbers of loop elements on a conformal surface, and these four arrays shared the similar coverages of coil configurations A, D, E and F as in Fig.1, respectively. All coil elements were modeled using conductors with 0.5mm-thickness and $1.26 \times 10^{-8} \Omega \cdot m$ resistivity. EM solver MARIE [53] was used again to simulate the corresponding SNR and g-factor for each array mounted on the same monkey head model. Each coil element was modeled with 2 segments (2 port). Co-simulation was performed for each element based on the S matrix generated in MARIE simulation, and each coil element was tuned and matched. Perfect inductance decoupling was assumed in coil array simulation. The spatial SNR of each array was calculated using the optimized combination method in SENSE reconstruction. G-factors were calculated with an in-plane acceleration rate of $R_{\text{SENSE}} = 3 \times 3$ along directions of F-H and A-P by assuming the macaque was placed in the prone position inside a horizontal MRI bore.

III. RESULT

Fig.2 shows the natural log of UISNR profiles on the central sagittal slice for all 7 coil-space configurations (upper row), and ratios of UISNR for coil-space configurations B-G vs. A (lower row), respectively. (Note that, by using 4,000 basis vectors, calculated UISNR were fully converged, which is shown in supporting Fig.S1 with the convergence plots¹). In general, most brain areas show similar UISNR profiles with different coil-to-object distances and coil-space geometries through comparing A with B-G. The most palpable changes in UISNR within the head result from differences in coil-space coverages. The uncovered lower and frontal part of the head by using helmet-like coil space, i.e., D-G, show significant lower UISNR than whole-head covered coil spaces, i.e., A-C. But, the surface region near the open-hole in coil space shows insignificant UISNR drop, as D vs. E. Increasing coil-to-object distance leads to significant drop in UISNR near the surface area and

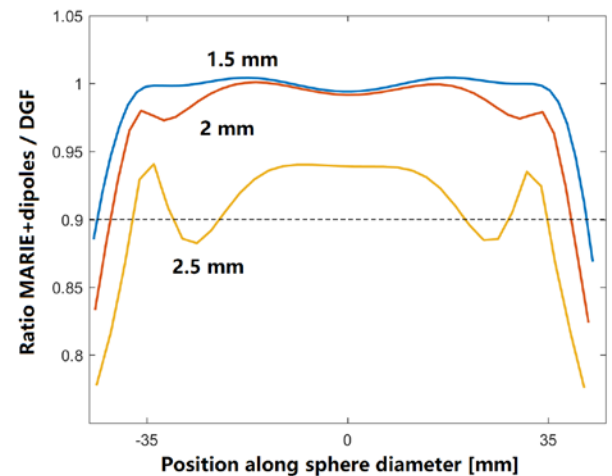


Fig.3. The impact of spatial resolution over the magnetic current contribution to UISNR on the agreement between the numerical UISNR method [50] and DGF-based analytical UISNR method [46]. The ratio between the two contributions were calculated over a 90mm-diameter sphere with an isotropic voxel resolution of 2.5mm, 2mm, and 1mm, respectively.

less significant drop in intermediate and deep areas, as A vs B and D vs F. Negligible changes over UISNR are observed for coil space with different thickness, as A vs. C and D vs. G.

Fig.3 shows a good consistency in calculations of magnetic current contribution by using dipole-cloud based numerical method [50] vs. the divergence-free current contribution (magnetic current type) by using the DGF-based analytical method [46]. More than 90% consistency can be ensured for most regions within the spherical model with an isotropic spatial resolution 2mm – higher spatial resolution leads to elevated consistency.

Fig.4 illustrates the dominance of magnetic current contribution to UISNR. (Note that, by using 4,000 basis vectors, calculated magnetic current contributions were fully converged, and the electric current contributions were fully converged too except in surface regions – the convergence plots are summarized in Fig.S1). In most brain regions for all coil-space configurations, magnetic current contributes higher than 90%

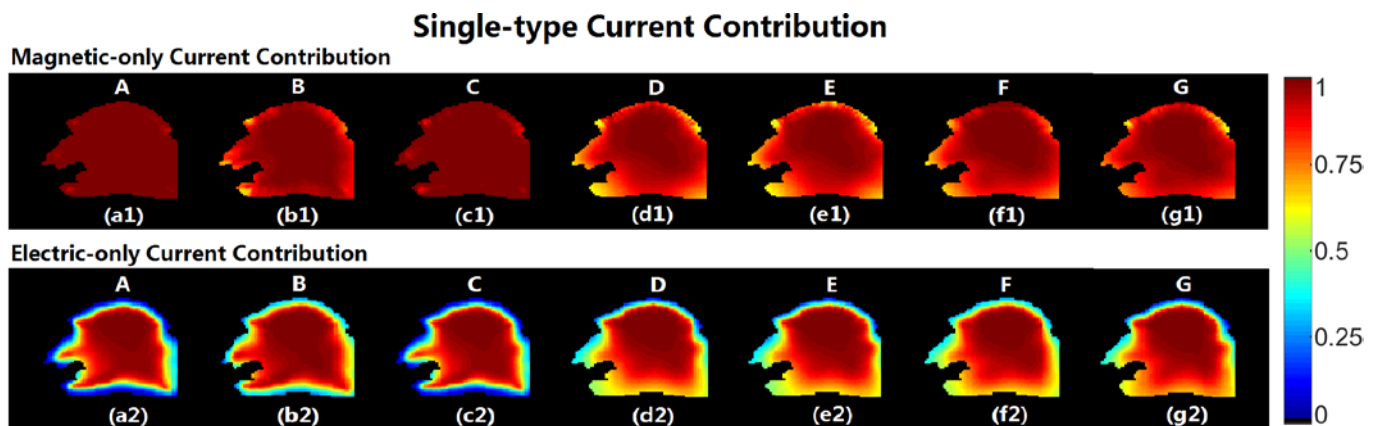


Fig.4. The sagittal views of the magnetic current contribution (upper row) and electric current contributions (lower row) to UISNR for each coil-space configuration, respectively.

¹ Supplementary materials are available in the supporting documents /multimedia tab.

of the UISNR. Moreover, decreasing the coil-space coverage will lead to decreased magnetic current contribution in coil space uncovered areas, as A vs. D, B vs. F, and C vs. G, respectively. No significant changes are observed through increasing coil-to-object distance, as A vs B and D vs E.

Fig. 5 shows the inverse uGF profiles on the center sagittal slice for each coil-space configuration under acceleration rates ranging from 2×2 to 6×6 (in-plane acceleration along F-H and A-P directions). Under the ultimate

case, configurations with whole-head coverage and 1cm coil-to-object distance (A and C) maintain an inverse g-factor higher than 0.8 in most cortical areas with an acceleration rate of up to 5×5 , while the helmet-like coverage and 1cm coil-to-object distance (D, E, and G) retain higher than 0.8 in most cortical areas with an acceleration rate of up to 4×4 . Either of increasing the coil-to-object distance (A vs. B, D vs. F) or decreasing coil-space coverage (A vs. D, B vs. F) will introduce significant drop in inverse uGF in both head surface and deep brain areas. Nevertheless, the existence of the opening ($28 \text{ mm} \times 28 \text{ mm}$) on top of the coil space (E) has negligible effect over the inverse uGF within the entire brain (D vs. E). The ultimate receive array with a thicker coil space shows similar but slightly lower inverse uGF than the ultimate receive array with thinner coil space, as C vs. A, and G vs. D, respectively. We further evaluated the magnetic current contribution to the UISNR with acceleration rates ranging from 2×2 to 6×6 (summarized in supporting Fig.S2), and found that the contribution maintains over 90% over the entire brain area.

Fig. 6 shows the actual SNR and inverse g-factor (3×3 in-plane acceleration) of realistic arrays I-IV (by using 3cm-diameter loop elements only) which resemble the coil-space configurations of A, D, E and F, respectively. Loop arrays constitute over 50% UISNR in most brain regions, and on the influences of coil-to-object distance and coil-space coverage over the resultant SNR and acceleration performance, simulation results show good agreement with the ultimate performance of the corresponding coil-space configurations. Moreover, all arrays show comparable SNR in the brain. In most brain regions, the SNR values of array II and III (helmet-like coverage) $\leq 80\%$ of SNR values of array I (whole-head coverage). Array IV with a larger coil-to-object distance introduces almost no degradation in SNR as compared with array II, but the cortical area near the coil opening of array III suffers obvious SNR drop compared with array II. Besides,

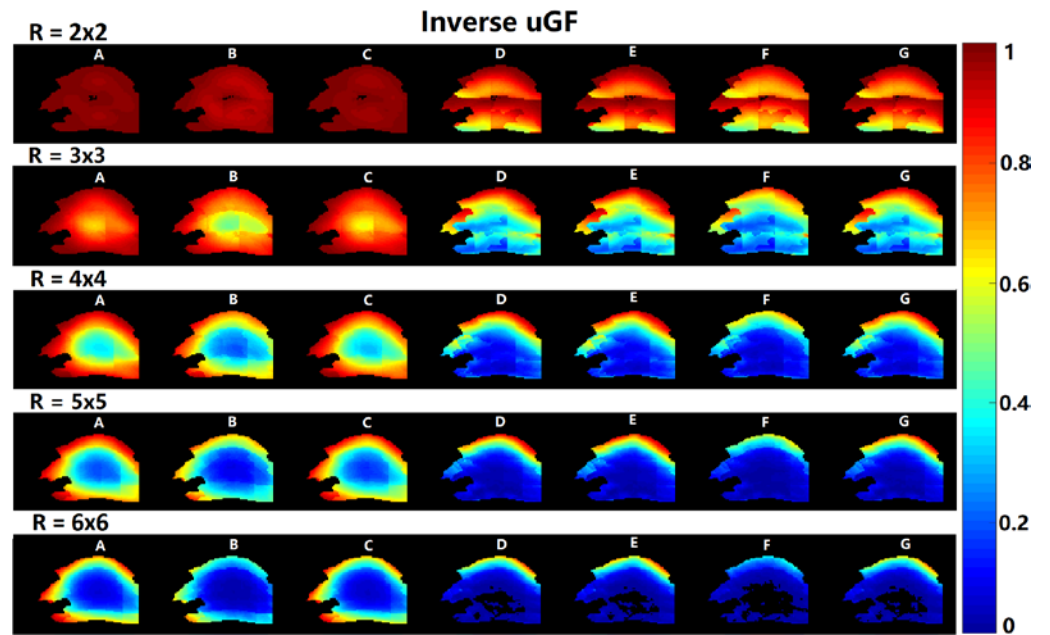


Fig.5. The sagittal views of the inverse uGF maps with in-plane accelerations ranging from 2×2 to 6×6 , respectively.

array I shows a much higher inverse g-factor profile in both cortical and deep brain regions: array I shows an inverse g-factor ≥ 0.8 in most deep brain regions and ≥ 0.9 in most cortical area, while array II and III exhibit ~ 0.8 near parietal and frontal lobes but ≤ 0.8 near the occipital lobe and deep brain regions, whereas array IV shows a much lower inverse g-factor in both cortical and deep brain regions.

IV. DISCUSSION

A. The influence of spatial constraints over UISNR

In this study, for the first time, we have theoretically demonstrated that the UISNR is independent of the coil-to-object distance when the Huygens's equivalence surface (coil space) is closed (i.e. with no spatial constraints); on the opposite, UISNR is dependent of the coil-to-object distance and coil-space coverage when the Huygens's equivalent surface is opened (i.e. with spatial constraints). Therefore, the coil-to-object distance, coil-space coverage and geometry of coil space should be carefully designed when studying the ultimate performance of coil arrays with opened coil space.

Initial attempt has been made by using opened analytical spherical surface to explore the influence of coil-space coverage on UISNR [59]. But the influence of these coil-space design parameters on ultimate coil performance has rarely been systematically investigated, especially on realistic models and with conformal coil spaces. Therefore, in this study, over a geometry-realistic monkey head model, the universal UISNR method [49,50] through Huygens's surface approximation, which is feasible to construct the spatial constrained conformal coil space on models with irregular geometries, is used to explore the influence of spatial constraints on the ultimate receive array performance.

B. The methodology of UISNR and uGF on realistic models

The agreement between calculated UISNR by using Huygens's surface approximation method vs. the well-established DGF method has been verified in previous study [46]. Based on it, to further explore whether loop coil elements alone can obtain sub-optimal SNR for opened coil space at 7T, we firstly verified the consistency between magnetic current contribution calculated by Huygens's surface approximation method vs. divergence-free current contribution by DGF method, for which the relationship between divergence-free current and the loop element has been well established [46,57,58]. Good agreement is observed (Fig.3) when using $\leq 2\text{mm}$ isotropic resolutions for both spherical model and spatial constrained Huygens's equivalent surface. Therefore, the magnetic current consisting of a large amount of discretized infinitesimal magnetic dipoles is able to explore the dominance of loop coil element. Furthermore, we also verified the convergence of UISNR and magnetic current contribution, and we found that a large amount ($>4,000$) of basis vectors is required to achieve a sufficient convergence in head surface areas (Fig.S1), which will inevitably cause elevated computation capability and time; nevertheless, the 4,000 basis vectors used in this study is adequate to demonstrate a good convergence in most brain regions.

The contribution of magnetic and electric currents on a uniform model has been systematically investigated using an analytical method [37]. In this study, we have presented the magnetic and electric current contributions on a model with realistic geometry. It is noteworthy that the magnetic and electric current contributions calculated in this study are not independent to each other as shown in Fig.4, although their source magnetic and electric dipoles are orthogonal with each other. Because the EM fields generated by magnetic and electric currents cannot be ensured to be orthogonal to each other due to field scattering, the noise covariance $\Psi_{N/2}^{E,M}$ and $\Psi_{N/2}^{M,E}$ are not equal to zero and, as a result, the contributions of magnetic and electric current are not independent to each other.

Because EM field basis vectors generated in realistic model are not usually orthogonal with each other, obvious noise

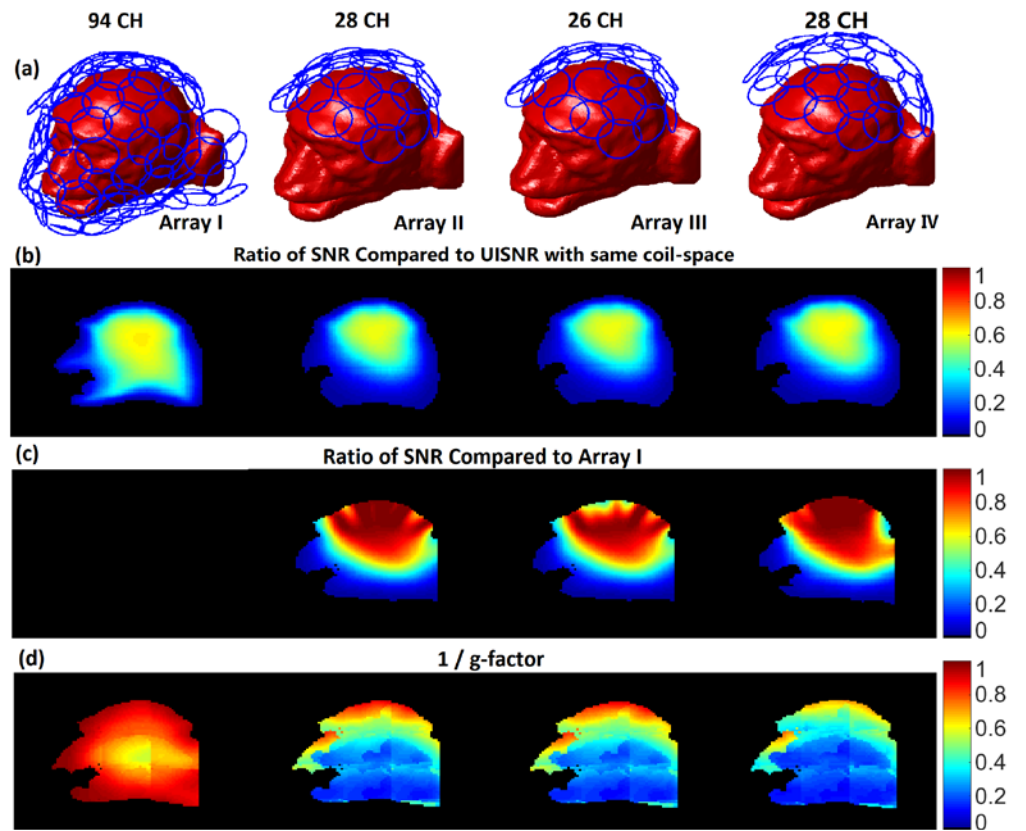


Fig.6. Simulation results of dense loop arrays I, II, III, and IV (a) which resemble coil configurations A, D, E, and F (shown in Fig.1), respectively. The ratio of the SNR vs. the corresponding UISNR profiles for each array is shown in (b), and the ratios of $\text{SNR}_{\text{Array II/III/IV}}$ vs. $\text{SNR}_{\text{Array I}}$ are shown in (c), respectively. With an in-plane acceleration of 3×3 , the inverse g-factor map of each array is shown in (d).

correlation exists between EM field basis vectors. However, in analytical UISNR studies, the noise covariance matrix is an identity matrix [37] due to the ideally orthogonal analytical basis set, which is equivalent to the fact that the ultimate g-factor is independent of noise covariance. Although the numerical method used in this study cannot generate ideally orthogonal EM field basis set, the EM field basis set with orthogonal fields still naturally exist. To simulate ultimate g-factor under ideal decoupling, we replaced noise co-variance matrix with identity matrix and kept the sensitivity matrix for g-factor evaluation.

C. Practical coil design guidelines for monkey brain imaging at 7T

In light of closed coil spaces that are impractical to construct in reality, compared to UISNR calculated using closed Huygens's surface, the spatial constrained ultimate coil performance with realistic coil-space geometry can provide more helpful insights and guidance for coil design. Up to now, the influence of coil-to-object distance and coil-space geometry has been investigated by using realistic coil elements and with finite channel numbers [59,60], but their ultimate performances have rarely been studied. Based on above simulation results, we tentatively conclude the following guidelines in RF coil design for monkey brain imaging at 7T:

1) SNR in brain region is insensitive to coil-to-object distance and coil-space coverage either under the ultimate or

realistic cases. As shown in Fig.2 and Fig.6, most brain regions show very similar SNR with different coil-to-object distances and coil-space coverages. Considering coil loss is ignored in UISNR and finite coil arrays simulated in this study are within the distance of sample noise dominate, the result can be partially accounted that both signal and sample noise are degraded with increasing coil-to-object distance. In addition, it should be emphasized that both ultimate intrinsic SNR and SNR of loop arrays are optimally combined; therefore, the optimally combined SNR performance of coil arrays may be less affected by variations in monkey head sizes, and the helmet coverage can be sufficient to provide enough SNR in brain region. However, it does not necessarily apply to sub-optimal combined SNR, e.g. root sum-of-square combined SNR, and cases with SNR combined in other sub-optimal way deserve further investigation. In the meantime, with increased coil-to-object distances, apparent UISNR drop is observed in head surface regions including the skin and bone, and it's because the numerical method used in this study has its inherent limitation in computation accuracy within superficial areas, which has been discussed in a previous report [50]. Higher resolution in computation model and larger number of current basis vectors are helpful to achieve higher computation accuracy in superficial areas, but it inevitably leads to higher requirement for computation resources and time. In this study, monkey brain is our primary region of interest, whereas the skin and bone in superficial areas are not, thus, a satisfactory convergence in the brain only would suffice our need of the present study.

2) Increasing coil-to-object distance will degrade the acceleration performance of coil arrays. Such degradation can be observed either in the ultimate case as A vs. B and D vs. F in Fig.5, or in practical array design examples as array II vs. IV in Fig.6, respectively. It suggests that the coil sensitive profiles generated from coil elements that are further away from the object is less distinctive regardless of the coil element size. For helmet-like arrays, to achieve reasonably good inverse g-factor profiles in cortical areas with an acceleration rate of 3×3 , keeping the coil-to-object distance within 1cm is advised.

3) Whole-head coverage is essential in achieving superior acceleration performances in deep brain regions either in the ultimate or realistic cases. Even under the ultimate cases, the helmet-like design is incapable of providing a satisfying inverse g-factor in deep brain regions with an acceleration rate of 3×3 (Fig.6). Therefore, to obtain a good acceleration performance in deep brain region, designs with the coil space approximating whole-head coverages and closely fitted to the object are preferred.

4) Headpost installation does not deteriorate the overall performance of the head array. As shown in Fig.2 and Fig.5, through comparing D vs. E, the existence of the coil opening ($28 \text{ mm} \times 28 \text{ mm}$) on top of the coil space has negligible influence over the UISNR and uGF; even in cases of realistic RF array design such as array II vs. III shown in Fig.6, its influence is still insignificant in most brain regions. Therefore, considering practical headpost installation in awake monkey MR experiments, head coils with coil openings should still

preserve satisfying performance in monkey brain imaging at 7T.

5) Loop element is optimal for monkey head array design at 7T. As evidenced by results shown in Fig.4, S1 and S2, the magnetic current component is sufficient to constitute of over 90% of UISNR in most brain regions (Fig.4), even with reduced coil-space coverages and high acceleration rates (Fig.S2).

D. Approaching the ultimate performance of monkey head arrays by using loop-only element at 7T

Theoretically, the ultimate performance of coil array can be achieved by using infinite infinitesimal coil elements with independent receive channels [44,45]. But coil elements with small dimensions appear to be coil-loss dominant, which cannot be practically implemented in realistic coil design. A number of studies have investigated this problem to find out to what extent a realistic coil array can achieve the ultimate performance [36,40,42,57]: dense loop arrays were studied in early years to explore such feasibility [40,42], and recently, single-type coil element or mixed-type coil elements with both magnetic and electric current components have been found to be essential to reach the ultimate performance at ultra-high magnetic field [36,57]. As discussed above, the magnetic current component is dominant in its contribution to the ultimate performance for monkey head coils at 7T, thus, coil arrays with dense loop elements were employed in this study: as illustrated in Fig.6, the 3cm-diameter loop element, which perhaps is with the smallest coil-loss dominant dimension for monkey head coil, was used to form four dense arrays, and the resultant SNR profiles can reach over 50% of the ultimate cases in many brain regions, while the inverse g-factor distributions resembling the ultimate performances closely, which suggests that current basis vectors with practical coil element dimension can provide enough spatial decoding capability. Note that such whole-head covered loop arrays can only constitute up to 60% of UISNR, and it can be explained as a result of modeled coil loss as well as co-simulation conducted during the numerical simulation procedures, which, on the contrary, are not considered in analytical UISNR calculations.

Considering the potential SNR improvement in both surface and deep regions of monkey brains at 7T, novel engineering methods that are capable of mitigating coil loss in small loop elements will be of great help to substantially advance the overall performance in state-of-the-art monkey coil designs.

V. CONCLUSION

In this study, the influences of coil-space design parameters, i.e., the coil-space coverage, coil-to-object distance, coil-element type, as well as the coil-space thickness, on spatial constrained ultimate coil performance have been evaluated based on the recently proposed numerical simulation method for universal UISNR and uGF. Besides, we have conducted additional simulations on coil arrays with finite number of loop elements to explore to what extent the ultimate coil performance can be achieved by using practical coil designs. Furthermore, from all above results, several guidelines on RF

coil design for monkey brain imaging at 7T have been tentatively concluded. Through our tentative efforts with numerical simulations, we hope to advance our understanding of the concept of UISNR towards practical considerations, and try to bridge the gap between theoretical analysis based on ultimate coil performance and realistic receive array design.

VI. ACKNOWLEDGMENT

We thank Dr. Gang Chen for assisting in macaque head model construction, Dr. Riccardo Lattanzi for providing the code of uniform sphere dyadic Green's function, and Drs. Bastien Guerin, Jonathan Polimeni and Larry Wald for useful discussions.

REFERENCES

- [1] S. Ogawa, T. Lee, A. Nayak and P. Glynn, "Oxygenation-sensitive contrast in magnetic resonance image of rodent brain at high magnetic fields," *Magnetic Resonance in Medicine*, vol. 14, pp. 68-78, 1990.
- [2] P. Bandettini, E. Wong, R. Hinks, R. Tikofsky and J. Hyde, "Time course EPI of human brain function during task activation," *Magnetic Resonance in Medicine*, vol. 25, pp. 390-397, 1992.
- [3] K. Kwong, J. Belliveau, D. Chesler, I. Goldberg, R. Weisskoff, B. Poncelet, D. Kennedy, B. Hoppel, M. Cohen and R. Turner, "Dynamic magnetic resonance imaging of human brain activity during primary sensory stimulation," *Proceedings of the National Academy of Sciences*, vol. 89, pp. 5675-5679, 1992.
- [4] N. Logothetis, H. Guggenberger, S. Peled and J. Pauls, "Functional imaging of the monkey brain," *Nature Neuroscience*, vol. 2, pp. 555-562, 1999.
- [5] E. Yacoub, A. Shmuel, J. Pfeuffer, P. Van De Moortele, G. Adriany, P. Andersen, J. Vaughan, H. Merkle, K. Ugurbil and X. Hu, "Imaging brain function in humans at 7 Tesla," *Magnetic Resonance in Medicine*, vol. 45, pp. 588-594, 2001.
- [6] R. S. Menon, S. Ogawa, J. P. Strupp, K. Ugurbil, "Ocular dominance in human v1 demonstrated by functional magnetic resonance imaging," *Journal of Neurophysiology*, vol. 77, pp. 2780-2787, 1997.
- [7] T. Q. Duong, D.-S. Kim, K. M. Ugurbil, and S.-G. Kim, "Spatiotemporal dynamics of the BOLD fMRI signals: Toward mapping submillimeter cortical columns using the early negative response," *Magnetic Resonance in Medicine*, vol. 44, pp. 231-242, 2000.
- [8] K. Cheng, R. Waggoner, and K. Tanaka, "Human Ocular Dominance Columns as Revealed by High-Field Functional Magnetic Resonance Imaging," *Neuron*, vol. 32, pp. 359-374, 2001.
- [9] E. Yacoub, A. Shmuel, N. Logothetis, and K. Ugurbil, "Robust detection of ocular dominance columns in humans using Hahn Spin Echo BOLD functional MRI at 7 Tesla," *NeuroImage*, vol. 37, pp. 1161-1177, 2007.
- [10] A. Shmuel, D. Chaimow, G. Raddatz, K. Ugurbil, and E. Yacoub, "Mechanisms underlying decoding at 7 T: Ocular dominance columns, broad structures, and macroscopic blood vessels in V1 convey information on the stimulated eye," *NeuroImage*, vol. 49, pp. 1957-1964, 2010.
- [11] J. B. Goense and N. K. Logothetis, "Laminar specificity in monkey V1 using high-resolution SE-fMRI," *Magnetic Resonance Imaging*, vol. 24, pp. 381-392, 2006.
- [12] G. Chen, F. Wang, J. C. Gore, and A. W. Roe, "Layer-specific BOLD activation in awake monkey V1 revealed by ultra-high spatial resolution functional magnetic resonance imaging," *NeuroImage*, vol. 64, pp. 147-155, 2013.
- [13] J. Polimeni, B. Fischl, D. Greve, and L. Wald, "Laminar analysis of high isotropic resolution BOLD activation with a resolution pattern stimulus in human V1 at 7T," *NeuroImage*, vol. 47, 2009.
- [14] S. G. Kim and K. Ugurbil, "Comparison of blood oxygenation and cerebral blood flow effect in fMRI: Estimation of relative oxygen consumption change," *Magnetic Resonance in Medicine*, vol. 38, pp. 59-65, 1997.
- [15] N. K. Logothetis, J. Pauls, M. Augath, T. Trinath, and A. Oeltermann, "Neurophysiological investigation of the basis of the fMRI signal," *Nature*, vol. 412, pp. 150-157, 2001.
- [16] T. Q. Duong, E. Yacoub, G. Adriany, X. Hu, K. Ugurbil, and S.-G. Kim, "Microvascular BOLD contribution at 4 and 7 T in the human brain: Gradient-echo and spin-echo fMRI with suppression of blood effects," *Magnetic Resonance in Medicine*, vol. 49, pp. 1019-1027, 2003.
- [17] L. M. Chen, G. H. Turner, R. M. Friedman, N. Zhang, J. C. Gore, A. W. Roe, and M. J. Avison, "High-Resolution Maps of Real and Illusory Tactile Activation in Primary Somatosensory Cortex in Individual Monkeys with Functional Magnetic Resonance Imaging and Optical Imaging," *Journal of Neuroscience*, vol. 27, pp. 9181-9191, 2007.
- [18] J. Pfeuffer, H. Merkle, M. Beyerlein, T. Steudel, and N. K. Logothetis, "Anatomical and functional MR imaging in the macaque monkey using a vertical large-bore 7 Tesla setup," *Magnetic Resonance Imaging*, vol. 22, pp. 1343-1359, 2004.
- [19] Y.-Y. I. Shih, Y.-Y. Chen, H.-Y. Lai, Y.-C. J. Kao, B.-C. Shyu, and T. Q. Duong, "Ultra high-resolution fMRI and electrophysiology of the rat primary somatosensory cortex," *NeuroImage*, vol. 73, pp. 113-120, 2013.
- [20] G. C. Wiggins, J. R. Polimeni, A. Potthast, V. Schmitt, V. Alagappan, and L. L. Wald, "96-Channel receive-only head coil for 3 Tesla: Design optimization and evaluation," *Magnetic Resonance in Medicine*, vol. 62, pp. 754-762, 2009.
- [21] B. Keil, G. C. Wiggins, C. Triantafyllou, L. L. Wald, F. M. Meise, L. M. Schreiber, K. J. Klose, and J. T. Heverhagen, "A 20-channel receive-only mouse array coil for a 3 T clinical MRI system," *Magnetic Resonance in Medicine*, vol. 66, pp. 582-593, 2011.
- [22] B. Keil and L. L. Wald, "Massively parallel MRI detector arrays," *Journal of Magnetic Resonance*, vol. 229, pp. 75-89, 2013.
- [23] N. Petridou, M. Italiaander, B. L. V. D. Bank, J. C. W. Siero, P. R. Luijten, and D. W. J. Klomp, "Pushing the limits of high-resolution functional MRI using a simple high-density multi-element coil design," *NMR in Biomedicine*, vol. 26, pp. 65-73, 2012.
- [24] R. Farivar, F. Grigorov, A. J. V. D. Kouwe, L. L. Wald, and B. Keil, "Dense, shape-optimized posterior 32-channel coil for submillimeter functional imaging of visual cortex at 3T," *Magnetic Resonance in Medicine*, vol. 76, pp. 321-328, 2015.
- [25] T. Janssens, B. Keil, P. Serano, A. Mareyam, J. A. McNab, L. L. Wald, and W. Vanduffel, "A 22-channel receive array with Helmholtz transmit coil for anesthetized macaque MRI at 3 T," *NMR in Biomedicine*, vol. 26, pp. 1431-1440, 2013.
- [26] G. Adriany, N. Harel, E. Yacoub, S. Moeller, G. Ghose, K. Ugurbil, "A 21 channel Transceiver Array for Non-human Primate Applications at 7 tesla," presented at the 18th Annu. Meet. ISMRM, Stockholm, Sweden, 2010, p. 1490.
- [27] A. Mareyam, J. Blau, J. Polimeni, B. Keil, R. Farivar, T. Benner, W. Vanduffel, and L. L. Wald, "Eight-channel array coil optimized for functional imaging of awake monkeys at 7T," presented at the 19th Annu. Meet. ISMRM, Montreal, Canada, 2011, p. 1823.
- [28] D. Papoti, C. C.-C. Yen, J. B. Mackel, H. Merkle, and A. C. Silva, "An embedded four-channel receive-only RF coil array for fMRI experiments of the somatosensory pathway in conscious awake marmosets," *NMR in Biomedicine*, vol. 26, pp. 1395-1402, 2013.
- [29] K. M. D. M. Gilbert, "Whole-brain and local receive arrays for imaging non-human primates," presented at the 21th Annu. Meet. ISMRM, Utah, USA, 2013, p.2776.
- [30] K. M. Gilbert, J. S. Gati, L. M. Klassen, P. Zeman, D. J. Schaeffer, S. Everling, and R. S. Menon, "A geometrically adjustable receive array for imaging marmoset cohorts," *NeuroImage*, vol. 156, pp. 78-86, 2017.
- [31] N. K. Logothetis, H. Merkle, M. Augath, T. Trinath, and K. Ugurbil, "Ultra High-Resolution fMRI in Monkeys with Implanted RF Coils," *Neuron*, vol. 35, pp. 227-242, 2002.
- [32] T. Janssens, B. Keil, R. Farivar, J. McNab, J. Polimeni, A. Gerits, J. Arsenault, L. Wald and W. Vanduffel, "An implanted 8-channel array coil for high-resolution macaque MRI at 3T," *NeuroImage*, vol. 62, , pp. 1529-1536, 2012.
- [33] J.-C. Ginefri, A. Rubin, M. Tatoulian, M. Woytasik, F. Boumezeur, B. Djemai, M. Poirier-Quinot, F. Lethimonnier, L. Darrasse, and E. Dufour-Gergam, "Implanted, inductively-coupled, radiofrequency coils fabricated on flexible polymeric material: Application to in vivo rat brain MRI at 7T," *Journal of Magnetic Resonance*, vol. 224, pp. 61-70, 2012.
- [34] G. C. Wiggins, B. Zhang, M. Cloos, E. Al, "Mixing loops and electric dipole antennas for increased sensitivity at 7 Tesla," presented at the 21th Annu. Meet. ISMRM, Utah, USA, 2013, p.2737.
- [35] G. Chen, K. Lakshmanan, D. Sodickson, and G. Wiggins, "A combined electric dipole and loop head coil for 7T head imaging," presented at the 23th Annu. Meet. ISMRM, Toronto, Canada, 2015, p.3133.

- [36] G. Chen, R. Lattanzi, D. Sodickson, and G. Wiggins. "Approaching the Ultimate Intrinsic SNR with Dense Arrays of Electric Dipole Antennas," *presented at the 24th Annu. Meet. ISMRM*, Singapore, 2016, p.168.
- [37] A. Pfrommer and A. Henning, "On the Contribution of Curl-Free Current Patterns to the Ultimate Intrinsic Signal-to-Noise Ratio at Ultra-High Field Strength," *NMR in Biomedicine*, vol. 30, 2017.
- [38] Y. Gao, W. Chen, J. Tian, Y. Sun, G. Chen, A. W. Roe, and X. Zhang. "Mixed Dipole and Loop Coil for Macaque Brain Imaging at 7T: A Simulation Study", *presented at the 25th Annu. Meet. ISMRM*, Honolulu, USA, 2017, p.4286.
- [39] M. A. Ertürk, A. J. Raaijmakers, G. Adriany, K. Ugurbil, and G. J. Metzger, "A 16-channel combined loop-dipole transceiver array for 7 Tesla body MRI," *Magnetic Resonance in Medicine*, vol. 77, pp. 884-894, 2016.
- [40] F. Wiesinger, N. D. Zanche and P. K. Pruessmann. "Approaching Ultimate SNR with Finite Coil Arrays," *presented at the 13th Annu. Meet. ISMRM*, Miami, Florida, USA, 2005, p.672.
- [41] A. M. Maunders, M. Daneshmand, P. Mousavi, B. G. Fallone, and N. D. Zanche, "Comparison of high-density composite and surface coil arrays for MRI of spherical imaging volumes," *presented at the IEEE MTT-S International Microwave Symposium*, Tampa, Florida, USA, 2014.
- [42] M. V. Vaidya, D. K. Sodickson, and R. Lattanzi, "Approaching ultimate intrinsic SNR in a uniform spherical sample with finite arrays of loop coils," *Concepts in Magnetic Resonance Part B: Magnetic Resonance Engineering*, vol. 44, pp. 53-65, 2014.
- [43] A. Pfrommer and A. Henning, "Optimal arrangement of finite element loop arrays for parallel magnetic resonance imaging in the human head at 400 MHz," *presented at the IEEE MTT-S International Microwave Symposium*, Phoenix, Arizona, USA, 2015.
- [44] M. A. Ohliger, A. K. Grant, and D. K. Sodickson, "Ultimate intrinsic signal-to-noise ratio for parallel MRI: Electromagnetic field considerations," *Magnetic Resonance in Medicine*, vol. 50, pp. 1018-1030, 2003.
- [45] F. Wiesinger, P. Boesiger, and K. P. Pruessmann, "Electrodynamics and ultimate SNR in parallel MR imaging," *Magnetic Resonance in Medicine*, vol. 52, pp. 376-390, 2004.
- [46] R. Lattanzi and D. K. Sodickson, "Ideal current patterns yielding optimal signal-to-noise ratio and specific absorption rate in magnetic resonance imaging: Computational methods and physical insights," *Magnetic Resonance in Medicine*, vol. 68, pp. 286-304, 2011.
- [47] A. Pfrommer and A. Henning, "On the Contribution of Curl-Free Current Patterns to the Ultimate Intrinsic Signal-to-Noise Ratio at Ultra-High Field Strength," *NMR in Biomedicine*, vol. 30, 2017.
- [48] A. Ishimaru, Wave propagation and scattering in random media. Piscataway, NJ: *IEEE Press*, 2005.
- [49] B. Guérin, J. F. Villena, A. G. Polimeridis, E. Al. "The ultimate SNR and SAR in realistic body models," *presented at the 22th Annu. Meet. ISMRM*, Milan, Italy, 2014, p.617.
- [50] B. Guérin, J. Villena, A. Polimeridis, E. Adalsteinsson, L. Daniel, J. White and L. Wald, "The ultimate signal-to-noise ratio in realistic body models", *Magnetic Resonance in Medicine*, vol. 78, pp. 1969-1980, 2016.
- [51] K. Pruessmann, M. Weiger, M. Scheidegger and P. Boesiger, "SENSE: Sensitivity encoding for fast MRI", *Magnetic Resonance in Medicine*, vol. 42, pp. 952-962, 1999.
- [52] C. Tai, Dyadic green functions in electromagnetic theory. *Oxford: Oxford University Press*, 1995.
- [53] A. Polimeridis, J. Villena, L. Daniel, and J. White, "Stable FFT-JVIE solvers for fast analysis of highly inhomogeneous dielectric objects," *Journal of Computational Physics*, vol. 269, pp. 280-296, 2014.
- [54] W. Chen, B. Peng, Y. Sun, G. Chen, A.W. Roe, Y. Dai, X. Zhang. "Subject-specific 3D modeling of macaque brain via automatic tissue registration based on in vivo MR images acquired at 7T," *presented at the 25th Annu. Meet. ISMRM*, Honolulu, USA, 2017, p.1280.
- [55] X. Zhang, P.-F. V. D. Moortele, S. Schmitter, and B. He, "Complex B1 mapping and electrical properties imaging of the human brain using a 16-channel transceiver coil at 7T," *Magnetic Resonance in Medicine*, vol. 69, pp. 1285-1296, 2012.
- [56] X. Zhang, S. Schmitter, P. V. D. Moortele, J. Liu, and B. He, "From complex B1 mapping to local SAR Estimation for human brain MR imaging using multi-channel transceiver coil at 7T," *IEEE Transactions on Medical Imaging*, vol. 32, pp. 1058-1067, 2013.
- [57] R. Lattanzi, G. C. Wiggins, B. Zhang, Q. Duan, R. Brown, and D. K. Sodickson, "Approaching ultimate intrinsic signal-to-noise ratio with loop and dipole antennas," *Magnetic Resonance in Medicine [Online]*, 2017.
- [58] C. M. Deniz, M. V. Vaidya, D. K. Sodickson, and R. Lattanzi, "Radiofrequency energy deposition and radiofrequency power requirements in parallel transmission with increasing distance from the coil to the sample," *Magnetic Resonance in Medicine*, vol. 75, pp. 423-432, 2015.
- [59] A. Pfrommer, A. Henning. "The ultimate intrinsic SNR in a spherical phantom with regard to an open-pole surface current distribution at 9.4T," *presented at the 25th Annu. Meet. ISMRM*, Honolulu, USA, 2017, p.749.
- [60] A. M. Maunders, M. Daneshmand, P. Mousavi, B. G. Fallone, and N. D. Zanche, "Comparison of high-density composite and surface coil arrays for MRI of spherical imaging volumes," *presented at the IEEE MTT-S International Microwave Symposium*, Tampa, Florida, USA, 2014.